







**Band energy dependence of defect formation in the topological semimetal Cd<sub>3</sub>As<sub>2</sub>**Chase Brooks <sup>1</sup>, Mark van Schilfgaarde <sup>2</sup>, Dimitar Pashov,<sup>3</sup> Jocienne N. Nelson,<sup>2</sup>  
Kirstin Alberi <sup>2</sup>, Daniel S. Dessau <sup>1</sup> and Stephan Lany <sup>2</sup><sup>1</sup>*Department of Physics, University of Colorado, Boulder, Colorado 80309, USA*<sup>2</sup>*National Renewable Energy Laboratory, Golden, Colorado 80401, USA*<sup>3</sup>*King's College London, The Strand, London WC2R 2LS, United Kingdom* (Received 23 November 2022; revised 23 February 2023; accepted 15 May 2023; published 29 June 2023)

Cadmium arsenide (Cd<sub>3</sub>As<sub>2</sub>) is a prototypical Dirac semimetal that manifests topological properties in a three-dimensional (3D) bulk material. In defect-free Cd<sub>3</sub>As<sub>2</sub>, the Fermi level  $E_F$  lies at a minimum in the density of states at the Dirac point, but experimentally it forms with excess electron carriers and an elevated  $E_F$ , thereby masking the topological features. To computationally study the self-doping of Cd<sub>3</sub>As<sub>2</sub>, we combine density functional theory (DFT) calculations for defect formation energies with quasiparticle self-consistent GW (QSGW) electronic structure calculations. We demonstrate an innate dependence of the point defect formation energies on carrier concentrations and use the QSGW calculated density of states to extrapolate formation energies to arbitrary electron concentrations. This approach allows the quantitative modeling of thermodynamic defect equilibria in topological semimetals and is used to predict how control of growth conditions might be utilized to achieve doping-neutral Cd<sub>3</sub>As<sub>2</sub>.

DOI: [10.1103/PhysRevB.107.224110](https://doi.org/10.1103/PhysRevB.107.224110)**I. INTRODUCTION**

Topological semimetals are an intriguing class of novel materials with a significant and sustained scientific interest. They are represented by several different compounds and exhibit a wide variety of transport and electronic structure phenomena as a consequence of their inherent symmetries, including ultrahigh electron mobility, large linear magnetoresistance, gapless bulk states, and linear band dispersion [1–5]. However, in real topological semimetal crystals, defects and impurities can cause doping and disorder, thereby constraining the accessibility of these topological features for application in next-generation devices. Cd<sub>3</sub>As<sub>2</sub> is a prototypical three-dimensional Dirac semimetal which is stable in ambient conditions unlike many of its alternatives [3,6]. The ground state is a centrosymmetric crystal structure derived from an underlying antiferroite lattice with an ordered sublattice of empty cation sites (space group 142,  $I4_1/acd$ ) [7]. Defect-free Cd<sub>3</sub>As<sub>2</sub> has a Fermi level that lies at a fourfold degenerate Dirac point along  $\Gamma$ -Z in the Brillouin zone (BZ) [7,8]. Unfortunately, Cd<sub>3</sub>As<sub>2</sub> crystal growth tends to induce unintentional  $n$ -type doping, so that the Fermi level  $E_F$  typically ends up about 100–200 meV above the Dirac point [9–12].

In this letter, we investigate computationally the role of intrinsic point defects in the self-doping behavior and examine how growth conditions of Cd<sub>3</sub>As<sub>2</sub> might be manipulated to tune  $E_F$  closer to the Dirac point and more readily access its topological features. Furthermore, our goal is to determine what computational methods beyond standard supercell approaches are necessary for an accurate representation of defect formation energies in a topological semimetal. Defect equilibrium calculations based on first-principles formation energies have a long history in semiconductors and insulators

[13], where they are applied to increasingly complex systems with disorder [14] and metastability [15]. Recent interest in such simulations for topological semimetals like TaAs [16] and Cd<sub>3</sub>As<sub>2</sub> in the present work motivates revisiting the issue of finite-size effects in supercell calculations in view of the absence of a band gap and the resulting differences in the screening behavior. We show that the dominant intrinsic point defects in Cd<sub>3</sub>As<sub>2</sub> (Cd interstitials and vacancies) can be modeled as fully ionized species in charge balance with electrons and hole carriers, and we present predictions for Fermi level control during synthesis.

**II. METHODS**

For total energy calculations, we use density functional theory (DFT) methods and perform supercell calculations of the intrinsic point defects, using the projector augmented wave (PAW) method as implemented in the VASP code [17,18], and utilizing both the generalized gradient approximation (GGA) of Ref. [19] and the strongly constrained and appropriately normed (SCAN) meta-GGA functional of Ref. [20]. Compared to standard DFT functionals, SCAN generally improves the prediction of lattice constants and avoids the systematic errors in the elemental reference energies [21]. To obtain an accurate electronic structure with high resolution BZ sampling, we perform quasiparticle self-consistent GW (QSGW) calculations with the Questaal code [22–24]. To obtain the alignment of the GW band energies relative to SCAN, we also performed eigenvalue self-consistent GW calculations [25] in VASP [26]. The final results include spin-orbit coupling in both total-energy and electronic structure calculations. More specific details for the individual calculations presented below are given in the Supplemental Material (SM).

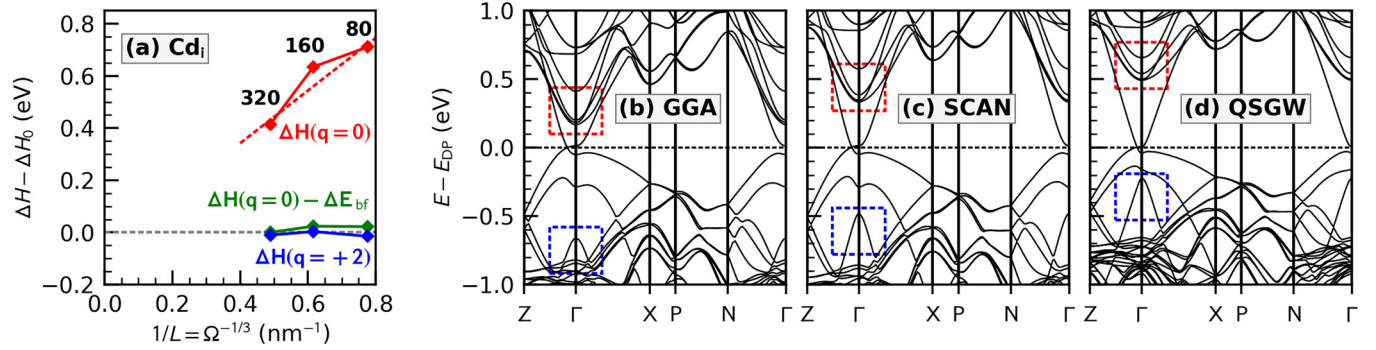


FIG. 1. (a) The supercell size dependence of the formation energy  $\Delta H$  of the  $\text{Cd}_i$  defect in  $\text{Cd}_3\text{As}_2$  as a function of inverse linear supercell size  $1/L = \Omega^{-1/3}$  obtained from supercell volume  $\Omega$ .  $\Delta H_0$  corresponds to the dilute limit of the formation energy. (b)–(d) The electronic band structure of  $\text{Cd}_3\text{As}_2$  with energies measured from the Dirac point energy  $E_{\text{DP}}$ , calculated with GGA (b), SCAN (c), and quasiparticle self-consistent GW theory (d). All band structures were calculated for the same atomic structure that was relaxed with the SCAN functional.

### III. FINITE-SIZE EFFECTS OF DEFECT FORMATION ENERGIES

First-principles calculations of point defects are most frequently performed using supercells under periodic boundary conditions. However, this approach can be subject to spurious interactions between the defect and its periodic images. The corrections necessary to extrapolate the formation energies to the dilute limit have been thoroughly investigated for band gap systems [27,28]. To investigate how these methods can be adopted to a Dirac semimetal like  $\text{Cd}_3\text{As}_2$ , and to define an approach for evaluating the defect formation energies in a defect equilibrium with varying defect and carrier concentrations, we first calculate the supercell size dependence for both electron and hole donating intrinsic defects.

In the supercell approach to defects in a solid, the formation energy of a defect  $D$  in a charge state  $q$  is given by

$$\Delta H_{D,q}(E_F, \{\mu\}) = [E_{D,q} - E_h] + \sum_{\alpha} n_{\alpha} \mu_{\alpha} + qE_F, \quad (1)$$

where  $E_{D,q}$  and  $E_h$  are the total energies of the defect and host supercells, respectively,  $\mu_{\alpha}$  are the chemical potentials of the atom species  $\alpha$  that are removed ( $n_{\alpha} = +1$ ) or added ( $n_{\alpha} = -1$ ) to the host crystal in forming the defect, and  $E_F$  is the Fermi energy. Here,  $E_F$  corresponds to the thermodynamic electron chemical potential, e.g., in a defect equilibrium, which is generally different from the Fermi level in the supercell calculation of a specific defect. The  $\text{Cd}_3\text{As}_2$  primitive cell has 80 atoms with 3 nonequivalent sites for each Cd and As and one empty cation site which we use as interstitial site.

Figure 1(a) shows the dependence of  $\Delta H_D$  of the charge-neutral ( $q = 0$ )  $\text{Cd}_i$  interstitial defect on the supercell size between 80 and 320 atoms (GGA level calculation without spin-orbit coupling). We observe strong finite-size effects for both the donor-type  $\text{Cd}_i$  [Fig. 1(a)] and the acceptor-type  $V_{\text{Cd}}$  (Fig. S1 in the SM) defects. This effect is expected because these defects alter the stoichiometry and electron count, but do not introduce localized defect states that would bind the two excess electrons ( $\text{Cd}_i$ ) or holes ( $V_{\text{Cd}}$ ). In this situation, the electrons (holes) introduced by the defect fill the band continuum of the host material and raise (lower) the Fermi energy, in analogy to “shallow” dopants in semiconductors [29]. In contrast to the Cd interstitials and vacancies, the As vacancy  $V_{\text{As}}$  acts analogous to “deep” dopants in the sense

that it does introduce localized defect states close to the Dirac point [9]. The implications of this different behavior for the absolute formation energies will be discussed below.

In case of the Cd defects, the concentration dependent change of  $E_F$  causes corresponding “band-filling” energies [29]

$$\Delta E_{\text{bf}} = \sum_{\substack{n, \mathbf{k} \\ \varepsilon_{n, \mathbf{k}} > E_{\text{DP}}}} w_{\mathbf{k}} f_{n, \mathbf{k}} (\varepsilon_{n, \mathbf{k}} - E_{\text{DP}}) \quad (2)$$

for electron donating defects ( $\text{Cd}_i$ ) and an analogous expression for electron accepting defects ( $V_{\text{Cd}}$ ). Using the occupancy  $f_{n, \mathbf{k}}$  of each band  $n$  at  $k$ -point  $\mathbf{k}$  with BZ weight  $w_{\mathbf{k}}$ , the sum in Eq. (2) and in the analogous equation for acceptors integrates the contributions of the band energies  $\varepsilon_{n, \mathbf{k}}$  of occupied states above (donors) or unoccupied states below (acceptors) the Dirac point energy  $E_{\text{DP}}$ , which plays the role of the reference value for the Fermi level of the undoped material. Here, the potential alignment technique of Ref. [30] is used to obtain consistent energy scales between defect and host cells. Subtracting the band-filling energies  $\Delta E_{\text{bf}}$  from  $\Delta H_D$ , we obtain formation energies that are in good approximation cell-size independent [Figs. 1(a) and S1].

In semiconductors or insulators, electron donating or accepting defects can form in a charged defect state when they exchange electrons with each other or with the band continuum of the host material. A similar mechanism is expected here as well, but there are important differences arising from the fact that  $\text{Cd}_3\text{As}_2$  does not have a band gap. While the detailed screening behavior of Dirac semimetals is still subject to active research [31], we expect that defect charges are fully screened in the long-distance limit. As a consequence, there is no bound state analogous to the hydrogenic level in effective-mass theory [32]: the neutral  $\text{Cd}_i^0$  essentially constitutes a charged  $\text{Cd}_i^{+2}$  defect with 2 electrons in the conduction-bandlike states above  $E_{\text{DP}}$ . To demonstrate this equivalence, Figs. 1(a) and S1 also include the size dependence for the charged defects, where the additional carriers are excluded from the calculation.

To remove spurious image charge interactions in case of charged defect supercell calculations, there are additional terms for the formation energies [Eq. (1)] needed to correct for the electrostatic interaction between the defect and

the compensating background [27,30,33]. This contribution depends on the dielectric constant and can exceed 1 eV in wide-gap systems [34,35]. In a topological semimetal, however, it should vanish for sufficiently large cell sizes. Indeed, for the largest 320 atom cell, we find that the formation energies of the band-filling corrected neutral (green) and the charged (blue) defects agree closely within about 0.01 eV [see Fig. 1(a)], for both the  $\text{Cd}_i^{+2}$  and  $V_{\text{Cd}}^{-2}$  defects. The more significant energy differences in the smaller cells are likely reflecting residual image charge interactions due to incomplete screening at shorter distances. Thus, from the cell size dependence in Fig. 1(a), we can estimate the screening length in  $\text{Cd}_3\text{As}_2$  as  $L \sim 2$  nm. We conclude then that  $\text{Cd}_i$  and  $V_{\text{Cd}}$  can be described as fully ionized defects, where the formation energy depends on the Fermi level [see Eq. (1)]. In this model, the contribution of band filling to  $\Delta H_{D,q}$  is encoded in the change of  $E_F$  with varying free carrier (electron or hole) concentrations [36].

#### IV. BAND ENERGY DEPENDENCE

Since the formation energies of defects at finite concentrations in  $\text{Cd}_3\text{As}_2$  depend innately on the electronic structure and density of states (DOS) near  $E_F$ , it is imperative that a quantitative description of its defects involves an accurate representation of the electron band energies. It is well known that the local approximation of standard DFT functionals leads to a significant underestimation of the band gap in insulating systems [37,38]. This limitation often has a considerable effect on calculated electronic properties and defect formation energies [27]. Similar problems exist for DFT calculations of topological materials: the approximation to the functional can give rise to quantitative errors in band dispersions [39,40], but it can also lead to an incorrect description of the overall band ordering [41,42]. DFT electronic structure errors must therefore be addressed when considering the  $\text{Cd}_3\text{As}_2$  Dirac semimetal band structure.

We performed QSGW calculations of  $\text{Cd}_3\text{As}_2$  in the 80-atom primitive cell to obtain an accurate model of the electronic structure. These QSGW results are shown alongside the band structures for both the GGA and SCAN functionals in Figs. 1(b)–1(d). There are several key features that distinguish the QSGW electronic structure from standard DFT. First, the Dirac point lies closer to the center of the Brillouin zone, and the band dispersion nearby is greater (a close-up of the band structure around the Dirac point is shown in Fig. S3). Second, the unoccupied  $s$ -like bands above the Dirac point (highlighted in red) are moved upward. Third, the QSGW calculation exhibits a strong upward shift of an occupied band below  $E_F$  (highlighted in blue). This band has a dominant As- $p$  like character throughout the BZ but becomes  $s$ -like at  $\Gamma$ , revealing its origin from the topological band inversion.

These modifications to the electronic structure are analogous to GW corrections of DFT band energies in semiconductors, which generally increase the energy separation of unoccupied  $s$ -like and occupied  $p$ -like states [23,25,43]. It is essential these corrections be included in the defect model for  $\text{Cd}_3\text{As}_2$  because the band energies near the Dirac point affect the formation energies of defects. We find that the SCAN functional partially accounts for each of the above

features, so that the SCAN band structure lies somewhere in between GGA and QSGW (see Fig. 1). To obtain the most accurate defect model, we will combine below the defect formation energies from supercell calculation in SCAN, with the DOS obtained from QSGW via high-resolution BZ integration (Fig. S3). This strategy is inspired by a similar approach that proved successful in semiconductors and insulators [34].

#### V. ABSOLUTE DEFECT FORMATION ENERGIES

In addition to an improved description of the band structure (Fig. 1) and the associated electronic density of states, GW calculations also allow us to determine the change in absolute band energies relative to the underlying DFT functional. In semiconductors and insulators, the corresponding conduction and valence band edge shifts have been shown to dramatically improve the formation energies of fully ionized defects calculated in DFT [34]. Similar corrections are necessary for  $\text{Cd}_3\text{As}_2$ : The DFT supercell calculations yield the formation energies for the charged defects using the Dirac point  $E_{\text{DP}}$  as a reference energy for the Fermi level. In so far the GW calculation alters  $E_{\text{DP}}$  on an absolute scale, the Fermi level must follow suit to maintain the correct charge balance, thereby affecting the formation energies according to Eq. (1). To determine the shift of  $E_{\text{DP}}$ , we performed GW calculations of  $\text{Cd}_3\text{As}_2$  in which the wavefunctions, and hence the electron density and electrostatic potential, of the DFT-SCAN functional are maintained. The resulting shift of the reference energy is determined as  $\Delta E_{\text{DP}} = -0.19$  eV, which we include in the calculation of the formation energies via Eq. (1).

The defect energies depend on synthesis conditions through the chemical potentials  $\mu_\alpha = \mu_\alpha^0 + \Delta\mu_\alpha$  of Cd and As, observing  $\Delta H_f = 3\Delta\mu_{\text{Cd}} + 2\Delta\mu_{\text{As}} = -0.59$  eV/fu, where  $\mu_\alpha^0$  are the energies of the elemental solids and  $\Delta H_f$  is the calculated formation enthalpy of  $\text{Cd}_3\text{As}_2$  per formula unit (fu). Considering CdAs and  $\text{CdAs}_2$  as potential competing phases, we find that the Cd-rich limit is given by phase coexistence with Cd metal ( $\Delta\mu_{\text{Cd}} = 0$ ,  $\Delta\mu_{\text{As}} = -0.30$  eV) and the As-rich limit by coexistence with  $\text{CdAs}_2$  ( $\Delta\mu_{\text{Cd}} = \Delta\mu_{\text{As}} = -0.12$  eV), whereas CdAs lies slightly above the convex hull.

Figure 2 shows the formation energies for the energetically most favorable, fully ionized defects as a function of  $E_F$ , where we calculated the energies of all elements, compounds, and defects using the SCAN functional with spin-orbit coupling. In contrast to the two Cd defects described above, the As vacancy  $V_{\text{As}}$  introduces a localized defect state close to the Dirac point (see SM, Fig. S2c), which can be fully occupied ( $q = -1$ ), half occupied ( $q = 0$ ), or empty ( $q = +1$ ). The neutral state turns out to be slightly unstable (“negative-U defect” [44]), resulting in a (+/−) charge transition level at  $E_{\text{DP}} + 0.15$  eV in the formation energy diagram in Fig. 2. Overall, the formation energies of  $V_{\text{As}}$  are higher than those of  $\text{Cd}_i$  and  $V_{\text{Cd}}$  throughout the range of chemical potentials. Therefore, the net doping will be largely determined by the balance between the Cd interstitial and vacancy defects. The numerical values of the defect energies  $\Delta H_D$  for all nonequivalent sites are given in Table S1. The formation energies for the  $\text{As}_{\text{Cd}}$  and  $\text{Cd}_{\text{As}}$  antisite and the  $\text{As}_i$  interstitial defects

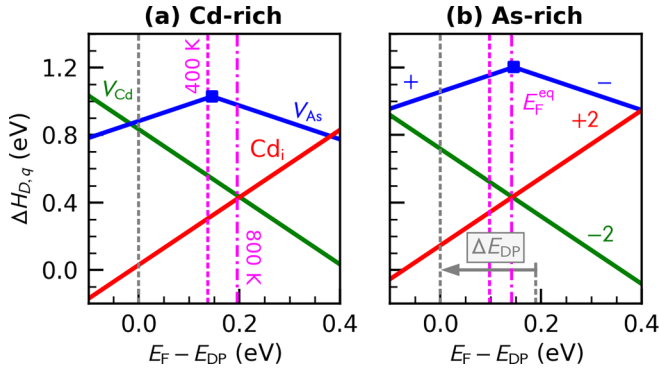


FIG. 2. Formation energies  $\Delta H_{D,q}$  of the intrinsic point defects in  $\text{Cd}_3\text{As}_2$  as a function of Fermi level  $E_F$  in (a) Cd-rich and (b) As-rich conditions. Only the lowest energy Wyckoff positions are shown for  $V_{As}$  and  $V_{Cd}$ . The GW correction  $\Delta E_{DP} = -0.19$  eV and equilibrium Fermi level  $E_F^{eq}$  for growth at  $T_g = 400$  K and 800 K are indicated.

were calculated for completeness. As seen in Fig. S2, they are sufficiently high to exclude them from the following analysis.

## VI. DEFECT EQUILIBRIA

It remains an open question how competing point defects collectively impact the properties of experimentally grown  $\text{Cd}_3\text{As}_2$ . We therefore consider a defect equilibrium and investigate the combined effect of all of the contributing defects simultaneously. For this thermodynamic equilibrium, we assume an initial growth temperature and calculate the associated defect concentrations as a function of the Cd and As chemical potentials, following a procedure similar to Refs. [45,46]. For the relatively dilute defect concentrations expected here, the defect concentrations in equilibrium at a temperature  $T$  are given by

$$c_{D,q}(E_F, \{\mu\}, T) = N_D e^{-\Delta H_{D,q}(E_F, \{\mu\})/k_B T}, \quad (3)$$

where  $N_D$  is the concentration of the atomic site where the defect  $D$  substitutes,  $k_B$  is the Boltzmann constant, and  $\Delta H_{D,q}(E_F, \{\mu\})$  contains the implicit  $E_F$  dependence as given by Eq. (1) above.

The defect equilibrium requires self-consistency between the defect densities  $c_{D,q}$  and the Fermi level  $E_F$  while simultaneously observing overall charge balance between defect charges and the carrier concentrations. To accurately account for the band-filling effects discussed above and to obtain the corresponding relationship between  $E_F$  and the carrier concentrations, we integrate the DOS  $g_{\text{QSGW}}(E)$  from the QSGW calculation, weighted with the Fermi-Dirac distribution, i.e.,

$$n_e = \int_{E_{DP}}^{\infty} \frac{g_{\text{QSGW}}(E)}{e^{(E-E_F)/k_B T} + 1} dE, \quad (4)$$

for electrons and, analogously,  $n_h$  for holes. The integration is facilitated by using a model function (see SM).

Experimentally,  $\text{Cd}_3\text{As}_2$  is grown in either bulk or thin film form. Molecular Beam Epitaxy (MBE) has been proven as a valuable tool for growth of high-quality  $\text{Cd}_3\text{As}_2$  with good control over the elemental chemical potentials [9,47,48]. MBE has a growth temperature window of about  $T_g \approx 110 - 250^\circ$ , where the upper limit results from the mod-

TABLE I. Defect equilibria for  $\text{Cd}_3\text{As}_2$  obtained from first-principles defect formation energies. Given are the concentrations  $c_D$  of the intrinsic defects and the resulting net doping  $c_{nd}$  depending on the growth temperature  $T_g$  and the Cd- or As-rich condition.

Cd/As rich	$T_g$ (K)	$c_D$ ( $\text{cm}^{-3}$ )				$c_{nd}$ ( $\text{cm}^{-3}$ )
		$\text{Cd}_i$	$V_{Cd}$	$V_{As}$		
Cd	400	$1.0 \times 10^{18}$	$8.2 \times 10^{14}$	$1.3 \times 10^9$	$2.0 \times 10^{18}$	
	600	$3.0 \times 10^{18}$	$1.2 \times 10^{18}$	$3.0 \times 10^{13}$	$3.7 \times 10^{18}$	
	800	$1.6 \times 10^{19}$	$1.5 \times 10^{19}$	$4.6 \times 10^{15}$	$2.9 \times 10^{18}$	
As	400	$3.5 \times 10^{17}$	$2.4 \times 10^{15}$	$2.2 \times 10^7$	$6.9 \times 10^{17}$	
	600	$2.1 \times 10^{18}$	$1.7 \times 10^{18}$	$1.0 \times 10^{12}$	$9.1 \times 10^{17}$	
	800	$1.5 \times 10^{19}$	$1.6 \times 10^{19}$	$3.6 \times 10^{14}$	$-2.7 \times 10^{18}$	

est formation enthalpy  $\Delta H_f$  (see above) and the fugacity of the atomic and molecular species. On the other hand, bulk synthesis can reach temperatures above  $400^\circ$  [12,49]. Thus, we consider here a range between 400 and 800 K for the calculations of defect equilibria.

The resulting defect concentrations are given in Table I and include a sum over all Wyckoff sites for  $V_{Cd}$  and  $V_{As}$  as well as a sum over the different charge states of  $V_{As}$ . As expected from the formation energies, the  $\text{Cd}_i$  and  $V_{Cd}$  defects are dominant and the concentrations of the As vacancies are several orders of magnitude lower. On account of the charge balance condition, the equilibrium Fermi level  $E_F^{eq}$  at  $T_g$  lies close to the intersection point between the  $\text{Cd}_i$  and  $V_{Cd}$  formation energies (Fig. 2). Table I also shows the net doping concentrations  $c_{nd} = 2[c_D(\text{Cd}_i) - c_D(V_{Cd})]$ , indicating that  $n$ -type growth ( $c_{nd} > 0$ ) is favored, as expected, under Cd-rich conditions for the full range of  $T_g$ . Interestingly, however,  $\text{Cd}_3\text{As}_2$  becomes net  $p$ -type ( $c_{nd} < 0$ ) at the higher end of growth temperatures under As-rich conditions. This transition suggests the intriguing possibility of doping-neutral growth of  $\text{Cd}_3\text{As}_2$ .

To elucidate the physical origin of the doping-type inversion, we study in more detail the temperature dependence of the Fermi level, shown in Fig. 3(a) for three different growth temperatures (circles). Both the asymmetry of the DOS (see Fig. S3 showing a much larger DOS below  $E_{DP}$

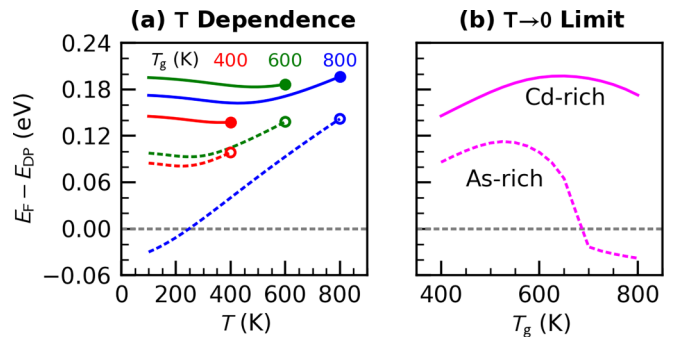


FIG. 3. (a) Temperature dependence of  $E_F$  in the presence of defect concentrations determined for three different growth temperatures  $T_g$  (circles). (b) Low temperature limit of  $E_F$  as a function of  $T_g$ . Solid and dashed lines indicate Cd-rich and As-rich conditions, respectively.

than above) and the width of the Fermi-Dirac distribution play important roles in determining the position of  $E_F^{\text{eq}}$ . At higher temperatures, their combined effect is to add positive charge from hole carriers even when  $E_F$  lies above  $E_{\text{DP}}$ . To maintain charge balance,  $E_F$  is pushed further upwards, which favors the formation of negatively charged acceptor-type defects (cf. Fig. 2). As a result, the net doping  $c_{\text{nd}}$  can become negative (cf. Table I).

For accessing the topological band-structure features of  $\text{Cd}_3\text{As}_2$ , the position of  $E_F$  at low temperature matters more than that at  $T_g$ . To model the  $T$  dependence of the electronic system, we reevaluate the charge-balance condition with the Fermi-Dirac distribution [Eq. (4)], while keeping the defect and corresponding net doping concentrations from the equilibrium at  $T_g$ . (At this point, Cd vacancies and interstitials could recombine if at least one of the species is mobile at the respective temperature. However, since the net doping,  $E_F$ , and the electron and hole concentrations are not affected by such recombination events, this effect is not explicitly modeled.) Figure 3(a) shows the resulting Fermi level  $E_F(T)$ , and the associated carrier concentrations  $n_e(T)$  and  $n_h(T)$  are shown in Fig. S4. In the low temperature limit, the dominant carrier type approaches the net doping concentration ( $n_e \rightarrow c_{\text{nd}}$  or  $n_h \rightarrow -c_{\text{nd}}$ ). In the  $n$ -type case, we observe an interesting nonmonotonic behavior of  $E_F(T)$ . To maintain the charge balance, the Fermi level first decreases with  $T$ , reflecting the positive slope of the DOS above  $E_{\text{DP}}$  (Fig. S3). Above a certain temperature that depends on  $c_{\text{nd}}$ , it starts to increase again, reflecting the high- $T$  behavior and DOS asymmetry described above.

Figure 3(b) summarizes the  $E_F(T)$  modeling by showing the low- $T$  limit of  $E_F$  as a function of  $T_g$ . While Cd-rich growth results in  $n$ -type doping with  $E_F(0) > E_{\text{DP}}$  for the full range of  $T_g$ , a conversion to net  $p$ -type doping with  $E_F(0) < E_{\text{DP}}$  occurs around 700 K under the As-rich condition. Thus, our modeling results suggest that doping-neutral  $\text{Cd}_3\text{As}_2$  could be achieved through control of the growth process. There are, however, two potential experimental challenges: Maintaining sufficiently As-rich conditions may require considerable As overpressures at higher temperatures, and rapid thermal processing techniques may be needed to quench in the defect equilibrium at these conditions.

## VII. CONCLUSIONS

Building upon existing methods for semiconductors and insulators, we defined a computational approach for evaluating first-principles defect equilibria in  $\text{Cd}_3\text{As}_2$ . Several conclusions are more broadly relevant for topological semimetals:

due to electronic screening, there are no bound states akin to hydrogenic dopant levels. Nevertheless, defects can have well defined charge states depending on the position of the Fermi level in the band continuum. However, it is particularly important to distinguish electron occupation of defect states from occupation of the band continuum. The latter cases do not represent legitimate charge states of the defect and cause a spurious cell size and concentration dependence of the formation energy. Finally, the overall charge balance condition depends strongly on the shape of the density of states near the Fermi level, often requiring an accurate electronic structure method beyond DFT. In  $\text{Cd}_3\text{As}_2$ , mutually compensating Cd interstitials and vacancies are the dominant intrinsic defects, with the former being the source of unintentional  $n$ -type doping, whereas the concentration of As vacancies remains much lower. Neither of the Cd defects cause localized states close to the Dirac point, thereby allowing the Fermi level to penetrate the band continuum. Due to the absence of a band gap and the pronounced asymmetry in the DOS for electron and hole carriers, the defect equilibria exhibit strong and nonmonotonic temperature dependencies. The modeling leads to a prediction how doping-neutral  $\text{Cd}_3\text{As}_2$  could be grown, such that the Fermi level approaches the Dirac point in the low- $T$  limit.

The Supplemental Material [50] provides details of our computational methods and choice of model parameters, as well as auxiliary data on defect energies and density of states.

## ACKNOWLEDGMENTS

This research was performed under the project ‘‘Disorder in Topological Semimetals’’, funded by the U.S. Department of Energy (DOE), Office of Science (SC), Basic Energy Sciences, Physical Behavior of Materials program. The Alliance for Sustainable Energy, LLC, operates the National Renewable Energy Laboratory (NREL) for the DOE under Contract No. DE-AC36-08GO28308. The research used High-Performance Computing (HPC) resources of the National Energy Research Scientific Computing Center (NERSC), a DOE-SC user facility located at Lawrence Berkeley National Laboratory, operated under Contract No. DE-AC02-05CH11231. This research also used HPC resources at NREL, sponsored by DOE, Office of Energy Efficiency and Renewable Energy. We further acknowledge PRACE for awarding us access to JUWELS-Booster hosted by GCS@FZJ, Germany. The views expressed in the article do not necessarily represent the views of DOE or the U.S. Government.

- [1] L. M. Schoop, F. Pielhofer, and B. V. Lotsch, Chemical principles of topological semimetals, *Chem. Mater.* **30**, 3155 (2018).
- [2] P. Hosur and X. Qi, Recent developments in transport phenomena in Weyl semimetals, *C. R. Phys.* **14**, 857 (2013).
- [3] T. Liang, Q. Gibson, M. N. Ali, M. Liu, R. J. Cava, and N. P. Ong, Ultrahigh mobility and giant magnetoresistance in the Dirac semimetal  $\text{Cd}_3\text{As}_2$ , *Nat. Mater.* **14**, 280 (2015).

- [4] B. Singh, B. Ghosh, C. Su, H. Lin, A. Agarwal, and A. Bansil, Topological Hourglass Dirac Semimetal in the Nonpolar Phase of  $\text{Ag}_2\text{BiO}_3$ , *Phys. Rev. Lett.* **121**, 226401 (2018).
- [5] N. L. Nair, P. T. Dumitrescu, S. Channa, S. M. Griffin, J. B. Neaton, A. C. Potter, and J. G. Analytis, Thermodynamic signature of Dirac electrons across a possible topological transition in  $\text{ZrTe}_5$ , *Phys. Rev. B* **97**, 041111(R) (2018).

- [6] Z. K. Liu, J. Jiang, B. Zhou, Z. J. Wang, Y. Zhang, H. M. Weng, D. Prabhakaran, S. K. Mo, H. Peng, P. Dudin *et al.*, A stable three-dimensional topological Dirac semimetal  $\text{Cd}_3\text{As}_2$ , *Nat. Mater.* **13**, 677 (2014).
- [7] M. N. Ali, Q. Gibson, S. Jeon, B. B. Zhou, A. Yazdani, and R. J. Cava, The crystal and electronic structures of  $\text{Cd}_3\text{As}_2$ , the three-dimensional electronic analogue of graphene, *Inorg. Chem.* **53**, 4062 (2014).
- [8] A. M. Conte, O. Pulci, and F. Bechstedt, Electronic and optical properties of topological semimetal  $\text{Cd}_3\text{As}_2$ , *Sci. Rep.* **7**, 45500 (2017).
- [9] J. N. Nelson, I. A. Leahy, A. D. Rice, C. Brooks, G. Teeter, M. van Schilfgaarde, S. Lany, B. Fluegel, M. Lee, and K. Alberi, Direct link between disorder and magnetoresistance in topological semimetals, *Phys. Rev. B* **107**, L220206 (2023).
- [10] H. T. Chorsi, S. Yue, P. P. Iyer, M. Goyal, T. Schumann, S. Stemmer, B. Liao, and J. A. Schuller, Widely tunable optical and thermal properties of Dirac semimetal  $\text{Cd}_3\text{As}_2$ , *Adv. Opt. Mater.* **8**, 1901192 (2020).
- [11] G. S. Jenkins, C. Lane, B. Barbiellini, A. B. Sushkov, R. L. Carey, F. Liu, J. W. Krizan, S. K. Kushwaha, Q. Gibson, T.-R. Chang, H.-T. Jeng, H. Lin, R. J. Cava, A. Bansil, and H. D. Drew, Three-dimensional Dirac cone carrier dynamics in  $\text{Na}_3\text{Bi}$  and  $\text{Cd}_3\text{As}_2$ , *Phys. Rev. B* **94**, 085121 (2016).
- [12] R. Sankar, M. Neupane, S.-Y. Xu, C. Butler, I. Zeljkovic, I. Panneer Muthuselvam, F.-T. Huang, S.-T. Guo, S. K. Karna, M.-W. Chu *et al.*, Large single crystal growth, transport property and spectroscopic characterizations of three-dimensional Dirac semimetal  $\text{Cd}_3\text{As}_2$ , *Sci. Rep.* **5**, 12966 (2015).
- [13] S. B. Zhang and J. E. Northrup, Chemical Potential Dependence of Defect Formation Energies in GaAs: Application to Ga Self-Diffusion, *Phys. Rev. Lett.* **67**, 2339 (1991).
- [14] J. Pan, J. Cordell, G. J. Tucker, A. C. Tamboli, A. Zakutayev, and S. Lany, Interplay between composition, electronic structure, disorder, and doping due to dual sublattice mixing in nonequilibrium synthesis of  $\text{ZnSnN}_2\text{:O}$ , *Adv. Mater.* **31**, 1807406 (2019).
- [15] A. Goyal, A. Zakutayev, V. Stevanović, and S. Lany, Computational fermi level engineering and doping-type conversion of  $\text{Mg:Ga}_2\text{O}_3$  via three-step synthesis process, *J. Appl. Phys.* **129**, 245704 (2021).
- [16] J. Buckeridge, D. Jevdokimovs, C. R. A. Catlow, and A. A. Sokol, Nonstoichiometry and Weyl fermionic behavior in TaAs, *Phys. Rev. B* **94**, 180101(R) (2016).
- [17] P. E. Blöchl, Projector augmented-wave method, *Phys. Rev. B* **50**, 17953 (1994).
- [18] G. Kresse and D. Joubert, From ultrasoft pseudopotentials to the projector augmented-wave method, *Phys. Rev. B* **59**, 1758 (1999).
- [19] J. P. Perdew, K. Burke, and M. Ernzerhof, Generalized Gradient Approximation Made Simple, *Phys. Rev. Lett.* **77**, 3865 (1996).
- [20] J. Sun, A. Ruzsinszky, and J. P. Perdew, Strongly Constrained and Appropriately Normed Semilocal Density Functional, *Phys. Rev. Lett.* **115**, 036402 (2015).
- [21] C. J. Bartel, A. W. Weimer, S. Lany, C. B. Musgrave, and A. M. Holder, The role of decomposition reactions in assessing first-principles predictions of solid stability, *npj Comput. Mater.* **5**, 4 (2019).
- [22] D. Pashov, S. Acharya, W. R. L. Lambrecht, J. Jackson, K. D. Belashchenko, A. Chantis, F. Jamet, and M. van Schilfgaarde, Questaal: A package of electronic structure methods based on the linear muffin-tin orbital technique, *Comput. Phys. Commun.* **249**, 107065 (2020).
- [23] M. van Schilfgaarde, T. Kotani, and S. Faleev, Quasiparticle Self-Consistent GW Theory, *Phys. Rev. Lett.* **96**, 226402 (2006).
- [24] T. Kotani, M. van Schilfgaarde, and S. V. Faleev, Quasiparticle self-consistent GW method: A basis for the independent-particle approximation, *Phys. Rev. B* **76**, 165106 (2007).
- [25] S. Lany, Band-structure calculations for the  $3d$  transition metal oxides in GW, *Phys. Rev. B* **87**, 085112 (2013).
- [26] M. Shishkin and G. Kresse, Implementation and performance of the frequency-dependent GW method within the PAW framework, *Phys. Rev. B* **74**, 035101 (2006).
- [27] S. Lany and A. Zunger, Assessment of correction methods for the band-gap problem and for finite-size effects in supercell defect calculations: Case studies for ZnO and GaAs, *Phys. Rev. B* **78**, 235104 (2008).
- [28] C. Freysoldt, B. Grabowski, T. Hickel, J. Neugebauer, G. Kresse, A. Janotti, and C. G. Van de Walle, First-principles calculations for point defects in solids, *Rev. Mod. Phys.* **86**, 253 (2014).
- [29] C. Persson, Y.-J. Zhao, S. Lany, and A. Zunger,  $n$ -type doping of  $\text{CuInSe}_2$  and  $\text{CuGaSe}_2$ , *Phys. Rev. B* **72**, 035211 (2005).
- [30] S. Lany and A. Zunger, Accurate prediction of defect properties in density functional supercell calculations, *Modell. Simul. Mater. Sci. Eng.* **17**, 084002 (2009).
- [31] M. N. Chernodub and M. A. H. Vozmediano, Direct measurement of a beta function and an indirect check of the Schwinger effect near the boundary in Dirac semimetals, *Phys. Rev. Res.* **1**, 032002(R) (2019).
- [32] H. Wang and A.-B. Chen, Calculation of shallow donor levels in GaN, *J. Appl. Phys.* **87**, 7859 (2000).
- [33] G. Makov and M. C. Payne, Periodic boundary conditions in ab initio calculations, *Phys. Rev. B* **51**, 4014 (1995).
- [34] H. Peng, D. O. Scanlon, V. Stevanovic, J. Vidal, G. W. Watson, and S. Lany, Convergence of density and hybrid functional defect calculations for compound semiconductors, *Phys. Rev. B* **88**, 115201 (2013).
- [35] H. Peng, D. O. Scanlon, V. Stevanovic, J. Vidal, G. W. Watson, and S. Lany, Addendum to Convergence of density and hybrid functional defect calculations for compound semiconductors *Phys. Rev. B* **96**, 239903(E) (2017).
- [36] S. Lany and A. Zunger, Dopability, Intrinsic Conductivity, and Nonstoichiometry of Transparent Conducting Oxides, *Phys. Rev. Lett.* **98**, 045501 (2007).
- [37] J. P. Perdew and M. Levy, Physical Content of the Exact Kohn-Sham Orbital Energies: Band Gaps and Derivative Discontinuities, *Phys. Rev. Lett.* **51**, 1884 (1983).
- [38] L. J. Sham and M. Schlüter, Density-Functional Theory of the Energy Gap, *Phys. Rev. Lett.* **51**, 1888 (1983).
- [39] L. Yang, J. Deslippe, C.-H. Park, M. L. Cohen, and S. G. Louie, Excitonic Effects on the Optical Response of Graphene and Bilayer Graphene, *Phys. Rev. Lett.* **103**, 186802 (2009).
- [40] I. Di Bernardo, J. Collins, W. Wu, J. Zhou, S. A. Yang, S. Ju, M. T. Edmonds, and M. S. Fuhrer, Importance of interactions for the band structure of the topological Dirac semimetal  $\text{Na}_3\text{Bi}$ , *Phys. Rev. B* **102**, 045124 (2020).

- [41] J. Vidal, X. Zhang, L. Yu, J.-W. Luo, and A. Zunger, False-positive and false-negative assignments of topological insulators in density functional theory and hybrids, *Phys. Rev. B* **84**, 041109(R) (2011).
- [42] I. Aguilera, C. Friedrich, and S. Blügel, Electronic phase transitions of bismuth under strain from relativistic self-consistent GW calculations, *Phys. Rev. B* **91**, 125129 (2015).
- [43] F. Aryasetiawan and O. Gunnarsson, The GW method, *Rep. Prog. Phys.* **61**, 237 (1998).
- [44] P. W. Anderson, Model for the Electronic Structure of Amorphous Semiconductors, *Phys. Rev. Lett.* **34**, 953 (1975).
- [45] S. Lany, Y.-J. Zhao, C. Persson, and A. Zunger, Halogen n-type doping of chalcopyrite semiconductors, *Appl. Phys. Lett.* **86**, 042109 (2005).
- [46] S. Lany, Communication: The electronic entropy of charged defect formation and its impact on thermochemical redox cycles, *J. Chem. Phys.* **148**, 071101 (2018).
- [47] T. Schumann, M. Goyal, H. Kim, and S. Stemmer, Molecular beam epitaxy of Cd<sub>3</sub>As<sub>2</sub> on a III-V substrate, *APL Mater.* **4**, 126110 (2016).
- [48] A. D. Rice, K. Park, E. T. Hughes, K. Mukherjee, and K. Alberi, Defects in Cd<sub>3</sub>As<sub>2</sub> epilayers via molecular beam epitaxy and strategies for reducing them, *Phys. Rev. Mater.* **3**, 121201(R) (2019).
- [49] I. Crassee, R. Sankar, W.-L. Lee, A. Akrap, and M. Orlita, 3D Dirac semimetal Cd<sub>3</sub>As<sub>2</sub>: A review of material properties, *Phys. Rev. Mater.* **2**, 120302 (2018).
- [50] See Supplemental Material at <http://link.aps.org/supplemental/10.1103/PhysRevB.107.224110> for technical details.